




Impact of nuclear structure on the background in the chiral magnetic effect in $^{96}_{44}\text{Ru} + ^{96}_{44}\text{Ru}$ and $^{96}_{40}\text{Zr} + ^{96}_{40}\text{Zr}$ collisions at $\sqrt{s_{NN}} = 7.7\text{--}200$ GeV from a multiphase transport model

Fei Li (李飞) ¹, Yu-Gang Ma (马余刚) ^{1,2,*}, Song Zhang (张松) ^{1,2}, Guo-Liang Ma (马国亮)^{1,2},
and Qiye Shou (寿齐烨)^{1,2,†}

¹Key Laboratory of Nuclear Physics and Ion-beam Application (MOE), Institute of Modern Physics, Fudan University, Shanghai 200433, China

²Shanghai Research Center for Theoretical Nuclear Physics, NSFC and Fudan University, Shanghai 200438, China



(Received 29 March 2022; revised 19 June 2022; accepted 1 July 2022; published 15 July 2022)

Impacts of nuclear structure on multiplicity (N_{ch}) and anisotropic flows (v_2 and v_3) in the isobaric collisions of $^{96}_{44}\text{Ru} + ^{96}_{44}\text{Ru}$ and $^{96}_{40}\text{Zr} + ^{96}_{40}\text{Zr}$ at $\sqrt{s_{NN}} = 7.7, 27, 62.4,$ and 200 GeV are investigated by using the string melting version of a multiphase transport (AMPT) model. In comparison with the experimental data released recently by the STAR Collaboration, it is found that the impact of quadrupole deformation β_2 on the v_2 difference is mainly manifested in the most central collisions, while the octupole deformation β_3 is in the near-central collisions, and the neutron skin effect dominates in the mid-central collisions. Viewing from the energy dependence, these effects are magnified at lower energies.

DOI: [10.1103/PhysRevC.106.014906](https://doi.org/10.1103/PhysRevC.106.014906)

I. INTRODUCTION

The present theories predict that a local parity (P) and charge-parity (CP) violation region could be formed by the strong interaction in relativistic heavy-ion collisions [1–4], where a charge number imbalance of light quarks can be achieved. In the process of a noncentral heavy-ion collision, the CP -violating region is affected by the strong magnetic field produced by high speed protons passing through [5,6], resulting in charge separation along the magnetic field. This phenomenon is also known as the chiral magnetic effect (CME) [7–11]. The confirmation of the existence of the CME will not only lead to a deeper understanding for QCD vacuum, but also imply the existence of the strong-interaction CP -violating region as well as the restoration of the chiral symmetry in quark gluon plasma (QGP). This phenomenon can be partly attributed to the influence of the strongest known electromagnetic field on the collision region [2,12,13]. Various anomalous chiral phenomena and possible detection methods have been discussed in literature, e.g., [13–21]. Finding an experimental signature that can conclusively confirm that the CME is one of the current major challenges in relativistic heavy-ion physics.

Since the magnetic field is usually perpendicular to the reaction plane (RP), defined by the impact parameter and the beam momentum in heavy-ion collisions, the CME-sensitive charge separation is measured with respect to the reaction plane, and the most widely used observable at present is the “ γ correlator”: $\gamma_{\alpha\beta} = \langle \cos(\phi_\alpha + \phi_\beta - 2\Psi_{RP}) \rangle$ [22], where ϕ_α and ϕ_β are the azimuthal angle of charged particles of

interest, and Ψ_{RP} is the angle of the reaction plane. However, some non-CME signal sources (e.g., local charge conservation and/or transverse momentum conservation entwined with the elliptic flow, v_2) can also contribute to the γ value, which makes it difficult to quantify the CME effect in this way [23–25].

In order to disentangle the contribution of non-CME background to γ , many ideas have been proposed, among which the isobar collisions (e.g., $^{96}_{44}\text{Ru} + ^{96}_{44}\text{Ru}$ and $^{96}_{40}\text{Zr} + ^{96}_{40}\text{Zr}$) are expected to provide the best solution to this problem. Since $^{96}_{44}\text{Ru} + ^{96}_{44}\text{Ru}$ and $^{96}_{40}\text{Zr} + ^{96}_{40}\text{Zr}$ have the same nucleon numbers but different charges, it is expected that different CME strengths can be quantitatively extracted from similar flow-driven backgrounds [26,27]. The experimental project of $^{96}_{44}\text{Ru} + ^{96}_{44}\text{Ru}$ and $^{96}_{40}\text{Zr} + ^{96}_{40}\text{Zr}$ isobar collisions at $\sqrt{s_{NN}} = 200$ GeV was launched at the BNL Relativistic Heavy Ion Collider (RHIC) in 2018, and the results were recently released by the STAR Collaboration [4]. The isobar blind analysis by the STAR Collaboration [28] showed significant differences in the multiplicity and flow harmonics in a given centrality between the two collision systems, indicating that the magnitude of the non-CME background is inconsistent between the two species. Many studies suggested that the discrepancy of CME backgrounds in Ru and Zr collisions was due to the different geometrical shapes of colliding ions, such as the difference of deformation and neutron skin thickness for Ru and Zr [26,29,30].

In this paper, the CME background difference between Ru and Zr collisions is studied using a multiphase transport (AMPT) model, with five configurations for the nuclear structure parameters of Ru and Zr. Our results are compared with the experimental data to verify which description for nucleon structure of Ru and Zr is more consistent with the realistic nuclear structure. Further, the energy dependence of the CME

*mayugang@fudan.edu.cn

†shouqiye@fudan.edu.cn

background differences between Ru and Zr is investigated at various energies, i.e. $\sqrt{s_{NN}} = 7.7, 27, 62.4, \text{ and } 200 \text{ GeV}$, aiming at probing the nature of the background at lower energies and providing theoretical support for future experiments.

The paper is organized as follows: In Sec. II, the general setup of modeling Ru+Ru and Zr+Zr collisions by AMPT is briefly introduced. In Sec. III, the numerical results and discussion are presented, and the summary is given in Sec. IV.

II. GENERAL SETUP

A. The AMPT model

Here we employed the string melting version of the AMPT model [31,32] to simulate Ru+Ru and Zr+Zr collisions and analyzed the generated data to study the CME backgrounds. The model has proved to be effective in describing collective flow in small and large collision systems at RHIC and at the CERN Large Hadron Collider (LHC) [33–37]. Based on the nonequilibrium transport dynamics, the AMPT model is composed of four parts: the heavy-ion jet interaction generator (HIJING) model [38,39] for generating the initial-state information, Zhang’s parton cascade (ZPC) model [40] for modeling partonic scatterings, the Lund string fragmentation model or a quark coalescence model for hadrons formation, and a relativistic transport (ART) model [41] for treating the hadron scatterings. In the AMPT model with the string melting mechanism, the partons freeze-out is according to local energy density and the hadronization process is simulated by a naive quark coalescence model, which combines two (three) nearest partons into a meson (baryon). The method for determining hadronic species is achieved by the flavor and invariant mass of coalescing partons.

B. Description of $^{96}_{44}\text{Ru}$ and $^{96}_{40}\text{Zr}$

The spatial distribution of nucleons in the rest frame of $^{96}_{44}\text{Ru}$ and $^{96}_{40}\text{Zr}$ can be described by the following two-parameter Fermi mass density of the Woods-Saxon (WS) form [26,42,43]:

$$\rho(r, \theta) = \frac{\rho_0}{1 + \exp\left[\frac{r - R_0[1 + \beta_2 Y_2^0(\theta) + \beta_3 Y_3^0(\theta)]}{a}\right]}, \quad (1)$$

where r is the radial position and θ is the polar angle in spherical coordinates, $\rho_0 = 0.16 \text{ fm}^{-3}$ is the nuclear saturation density, R_0 and a represent the “radius” of the nucleus and the surface diffuseness parameter, respectively, and the deformation of the nucleus is denoted by the most relevant axial symmetric quadrupole deformation β_2 and octupole deformation β_3 . Since the β_2 and β_3 values of $^{96}_{44}\text{Ru}$ and $^{96}_{40}\text{Zr}$ are not accurately known at present [26,44,45], here we take five sets of WS parameters which are suggested and used in heavy-ion collisions from recent references [46–51], as shown in Table I, to investigate the effect of nuclear structures on CME backgrounds for isobar collisions.

The parameters are arranged as follows: in Case 1, Ru ($\beta_2^{Ru} = 0.13$), has larger quadrupole deformation than Zr ($\beta_2^{Zr} = 0.06$); in Case 2, Ru ($\beta_2^{Ru} = 0.03$), in contrast, has a smaller quadrupole deformation than Zr ($\beta_2^{Zr} = 0.18$); Case 3 is based on the latest calculations of the energy

TABLE I. The Woods-Saxon parameters used in the AMPT model.

Nucleus	$^{96}_{44}\text{Ru}$				$^{96}_{40}\text{Zr}$			
	R (fm)	a (fm)	β_2	β_3	R (fm)	a (fm)	β_2	β_3
Case 1	5.13	0.46	0.13	0	5.06	0.46	0.06	0
Case 2	5.13	0.46	0.03	0	5.06	0.46	0.18	0
Case 3	5.067	0.5	0	0	4.965	0.556	0	0
Case 4	5.065	0.485	0.154	0	4.961	0.544	0.062	0.202
Case 5	5.09	0.46	0.162	0	5.02	0.52	0.06	0.20

density functional theory (DFT) [30,49], which assumes that the nucleus is spherical ($\beta_2 = 0$). According to the calculation of proton and neutron distribution, it shows that the overall size of Ru is smaller than that of Zr because the neutron skin of Zr is much thicker. Case 4 is also derived from the DFT result, but with recent research findings [50,51] for β_2 and β_3 , which gives a description of nuclear structure containing both the deformation effect and the neutron skin effect for $^{96}_{44}\text{Ru}$ and $^{96}_{40}\text{Zr}$. Case 5 is from the recent result [50], which also includes the deformation effect and the neutron skin effect. It should be noted that the neutron skin effect comes from the different density distributions of the proton and neutron, but in our computation the proton and neutron are identical in Case 3, Case 4, and Case 5, and the total nucleon density (the sum of the proton and neutron) is used to configure the initial nucleon coordinates. It has been proved in previous research [49] that the Ru+Ru/Zr+Zr ratio is almost the same for charged multiplicity distribution N_{ch} and the eccentricity ε_2 , which were calculated by the total nucleon density and the DFT density. This makes it possible to study the neutron skin effect by using the WS parameters of the total nucleon density. It has been proved in a recent work [50] that the effects of WS parameters on elliptic flow ratio of $v_{2,Ru}/v_{2,Zr}$ are as follows: (1) the v_2 ratio is mainly dominated by β_2 and to a minor extent by β_3 in the most-central collisions; (2) the v_2 ratio is influenced by a positive contribution from β_2 and a larger negative contribution from β_3 in the near-central collisions; (3) the influence of $\Delta a = a_{Ru} - a_{Zr}$ is manifested in the mid-central and peripheral collisions; and (4) and the impact of $\Delta R_0 = R_{0,Ru} - R_{0,Zr}$ only exists in the central collisions.

Figure 1 shows the distributions of charged hadron numbers from the AMPT model within $|\eta| < 0.5$ in Ru+Ru and Zr+Zr collisions at $\sqrt{s_{NN}} = 7.7, 27, 62.4, \text{ and } 200 \text{ GeV}$ for the above five sets of Woods-Saxon parameters. The multiplicity $P(N_{ch})$ of five cases perfectly matches the STAR multiplicity after multiplying by 1.21 (the same treatment was done in the work [51]) at $\sqrt{s_{NN}} = 200 \text{ GeV}$, and the ratio of Case 4 and the Case 5 gives the best description of the RHIC-STAR data [4]. It presents a similar distribution pattern at other energies in different N_{ch} regions. Based on the multiplicity distribution, the collision system is divided into different centralities for each set of the WS parameters. It is obvious that the N_{ch} interval of centralities class becomes more sensitive to the distribution for low multiplicity (peripheral collisions) at lower energy. Here the multiplicity N_{ch} is the number of particles at mid-pseudorapidity ($|\eta| < 0.5$) in the collisions.

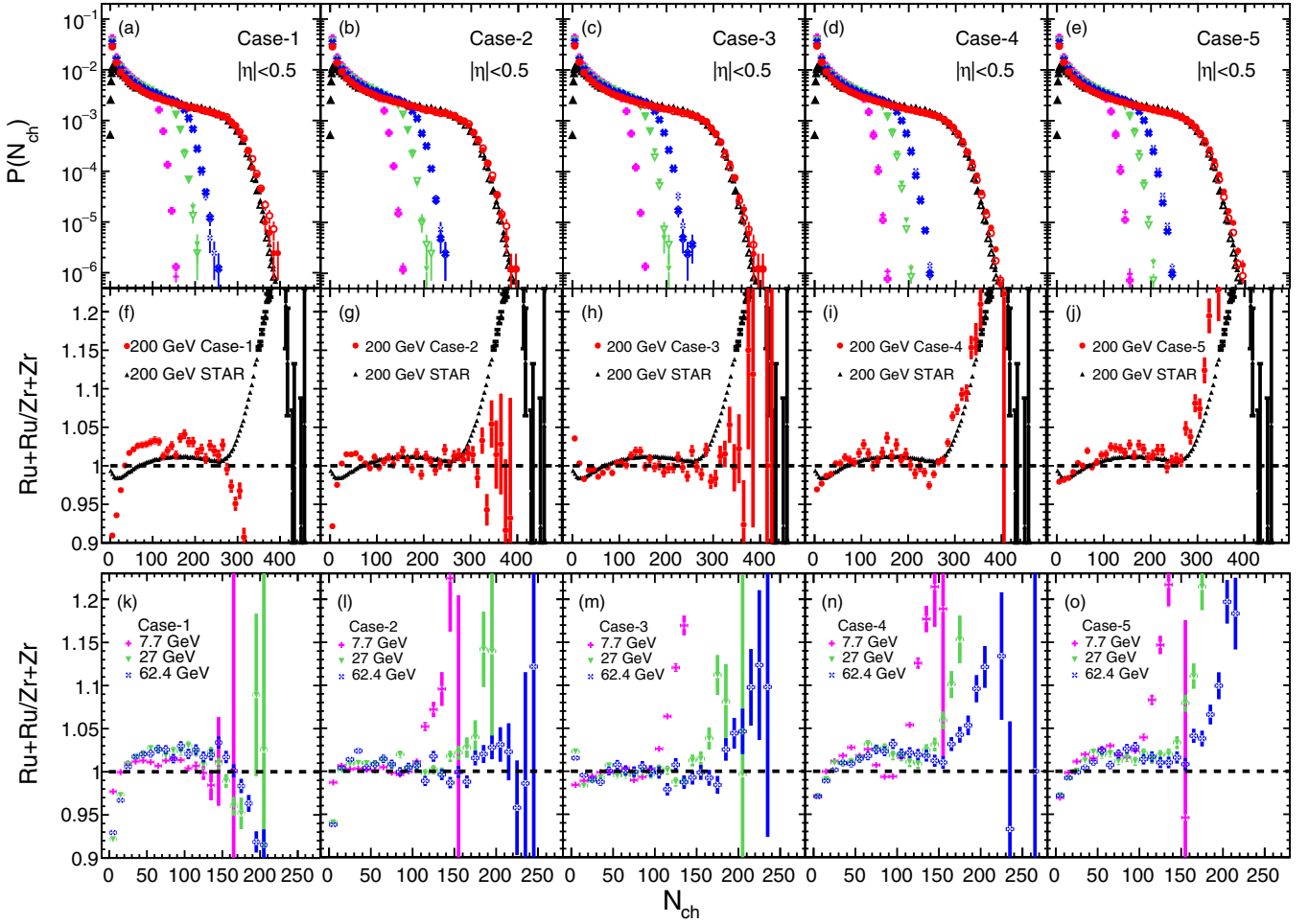


FIG. 1. Upper panels: Distributions of the number of charged hadrons from the simulation by AMPT in the pseudorapidity window $|\eta| < 0.5$ in Ru+Ru and Zr+Zr collisions at $\sqrt{s_{NN}} = 200$ GeV for five sets of Woods-Saxon parameters: (a) Case 1, (b) Case 2, (c) Case 3, (d) Case 4, and (e) Case 5. More details on definition of cases can be found in the text. The STAR data [4] for isobar collisions at $\sqrt{s_{NN}} = 200$ GeV are also shown for comparisons. Middle panels: The Ru+Ru to Zr+Zr ratios for five sets of Woods-Saxon parameters at $\sqrt{s_{NN}} = 200$ GeV, as well as the STAR data are shown, respectively. Lower panels: The Ru+Ru to Zr+Zr ratios for five sets of Woods-Saxon parameters at $\sqrt{s_{NN}} = 7.7, 27,$ and 62.4 GeV, respectively. Notice that the horizontal axis is zoomed in for clarity in the lower panels.

III. RESULTS AND DISCUSSION

In this section, the simulation results from the AMPT model for five nuclear density parameters of Ru+Ru and Zr+Zr collisions at $\sqrt{s_{NN}} = 7.7, 27, 62.4,$ and 200 GeV are presented. We will show the predictions for the mean multiplicity $\langle N_{ch} \rangle$, the elliptic flow v_2 , and the triangular flow v_3 of all particles as a function of centrality in the two isobaric collision systems. The effect of initial geometry on CME background will also be discussed according to the eccentricities in Ru+Ru and Zr+Zr collisions. The numbers of events we simulated for all cases for both $^{96}_{44}\text{Ru}$ and $^{96}_{40}\text{Zr}$ are, respectively, 5M (7.7 GeV), 2M (27 GeV), 2M (62.4 GeV), and 2.5M (200 GeV), where M denotes $\times 10^6$.

A. Mean charge multiplicity $\langle N_{ch} \rangle$

The upper panels of Fig. 2 show the mean charge multiplicity $\langle N_{ch} \rangle$ at mid-pseudorapidity ($|\eta| < 0.5$) as a function

of centrality, from the string melting mode of AMPT, for five cases of the parameter settings of isobar collision systems at $\sqrt{s_{NN}} = 7.7, 27, 62.4,$ and 200 GeV. The Ru+Ru/Zr+Zr ratio of the mean charge multiplicities is shown in the lower panels of Fig. 2. The STAR data [4] for isobar collision systems at $\sqrt{s_{NN}} = 200$ GeV are also shown for comparison. Our simulation results show that the mean charge multiplicities $\langle N_{ch} \rangle$ of the two isobar systems for five cases are close to each other, which is perfectly consistent with the data of the STAR Collaboration at different centralities.

The Ru+Ru/Zr+Zr ratio in the bottom panel of Fig. 2 gives a clear illustration of the difference between these two isobar collisions. The ratios for the five cases are different in shape, with Case 1 and Case 2 remaining close the unity for all centralities at different energies, and Case 3, Case 4, and Case 5 rising almost directly in proportion to the centrality at $\sqrt{s_{NN}} = 200$ GeV, and also rising in a zig-zag pattern at low energy. The shapes of the ratios in Case 3, Case 4 and Case

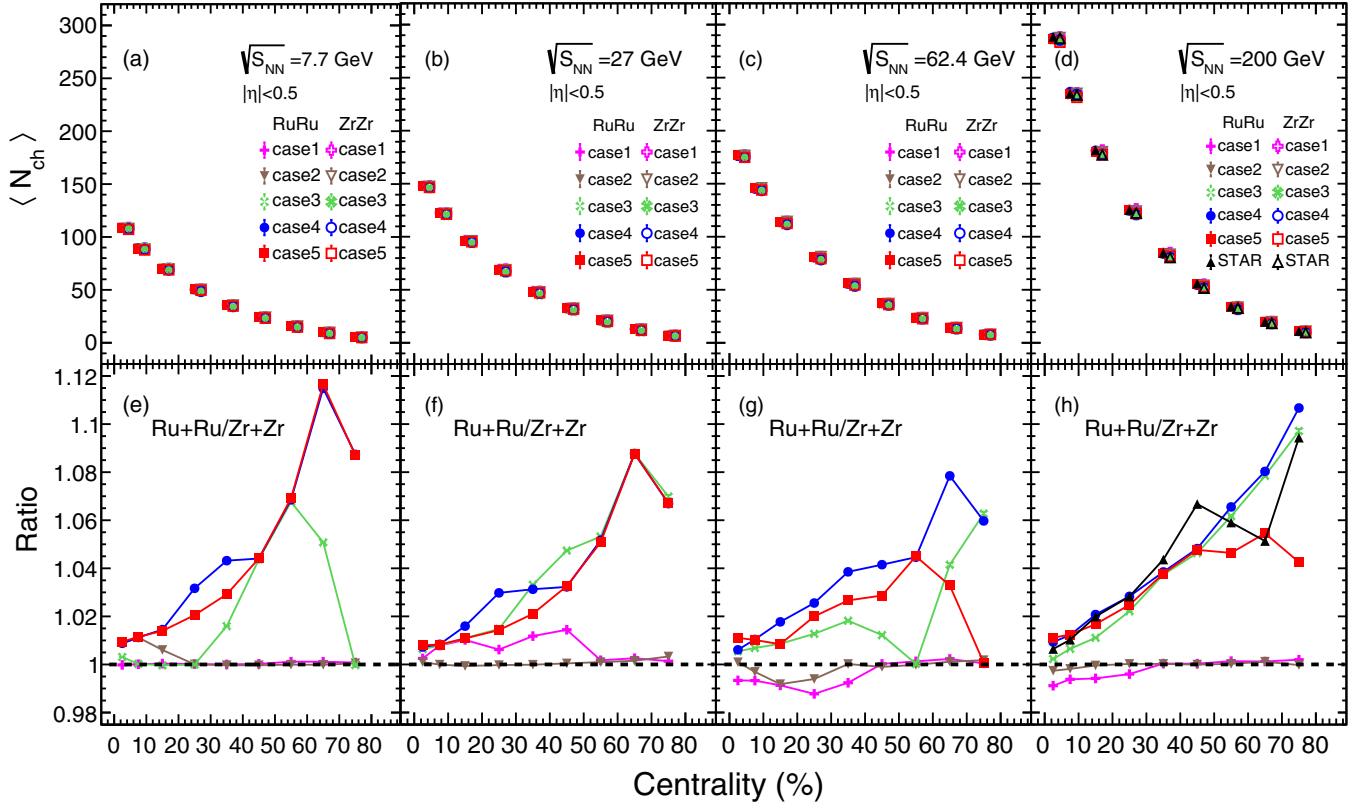


FIG. 2. Upper panels: The mean charge multiplicity N_{ch} within $|\eta| < 0.5$ as a function of centrality in Ru+Ru and Zr+Zr collisions at $\sqrt{s_{NN}} = 7.7, 27, 62.4,$ and 200 GeV. The STAR data [4] for isobaric collisions at $\sqrt{s_{NN}} = 200$ GeV are also shown for comparison. The centrality bins are slightly shifted for clarity. Lower panels: The ratio of the mean charge multiplicity in Ru+Ru collisions to that in Zr+Zr collisions with matching centrality and energy. The above data include statistical uncertainty.

5 are the closest to the STAR measurements at $\sqrt{s_{NN}} = 200$ GeV. This indicates that the neutron skin effect has the major contribution to the ratio of $\langle N_{ch} \rangle$.

One of the puzzling things about the $\langle N_{ch} \rangle$ ratio of STAR's data at $\sqrt{s_{NN}} = 200$ GeV is that there is a zig-zag pattern after 50% centrality, which is interestingly similar to how Case 3, Case 4 and Case 5 behave at low energy. The zig-zag ratio after 50% centrality is actually due to the fact that in low multiplicity events (i.e., in peripheral collisions) the N_{ch} interval for a specific centrality has a small difference between $^{96}_{44}\text{Ru}$ and $^{96}_{40}\text{Zr}$ [51]. In other word, the events in $^{96}_{44}\text{Ru}$ and $^{96}_{40}\text{Zr}$ collisions within the same centrality region have different multiplicity regions. This small multiplicity difference can result in the zig-zag fluctuations for some observables. As shown in Fig. 2, the ratio with zig-zag fluctuations appears before 50% centrality in low energy collisions, because low energy collisions contain more low multiplicity events. Reference [51] points out that the ratio of multiplicity $\langle N_{ch} \rangle$ depends on centrality significantly, but the ratio of v_2 dose not.

B. Harmonic flow

The harmonic flow is investigated for the two isobaric collision systems, and contributes as a major background of the CME-sensitive observables, such as $\Delta\gamma_{112}$. The harmonic flow coefficient $v_n\{2\}$ is calculated by the two-particle

correlation method in the following form [4]:

$$v_{n=2,3}^2\{2\} = \langle \cos(n\phi_1 - n\phi_2) \rangle. \quad (2)$$

Here we use all particles and a larger pseudorapidity range ($|\eta| < 2$) to calculate $v_n^2\{2\}$ for higher statistics, and the $\Delta\eta_{1,2}$ is set to 0.05 for $v_n^2\{2\}$ calculation. The nonflow effect, which can be suppressed by using a larger $\Delta\eta_{1,2}$ cut, does not affect the ratio essentially.

The upper panels of Fig. 3 present the AMPT results for the centrality dependence of elliptic flow $v_2\{2\}$ at mid-pseudorapidity ($|\eta| < 2$) with five geometry settings of isobaric collisions. It can be seen that $v_2\{2\}$ for Ru+Ru and Zr+Zr are similar to each other at different energies, and the $v_2\{2\}$ with five setting parameters are also close to each other. Our results are consistent with the STAR data at $\sqrt{s_{NN}} = 200$ GeV, but slightly higher than that of the STAR data in central collisions.

The lower panels of Fig. 3 give the $v_2\{2\}$ ratios between Ru+Ru and Zr+Zr collisions. The centrality dependences of the ratios for the five settings are very different at $\sqrt{s_{NN}} = 200$ GeV: for Case 1 (2) the ratio decreases (increases) from central to peripheral collisions until about 20% centrality, staying close to unity, for Case 3 it shows as a bow above unity, and for Case 4 and Case 5 it shows the almost same shape as the STAR data. As seen from Case 1 and Case 2, the quadrupole deformation has a major effect on the $v_2\{2\}$ ratios

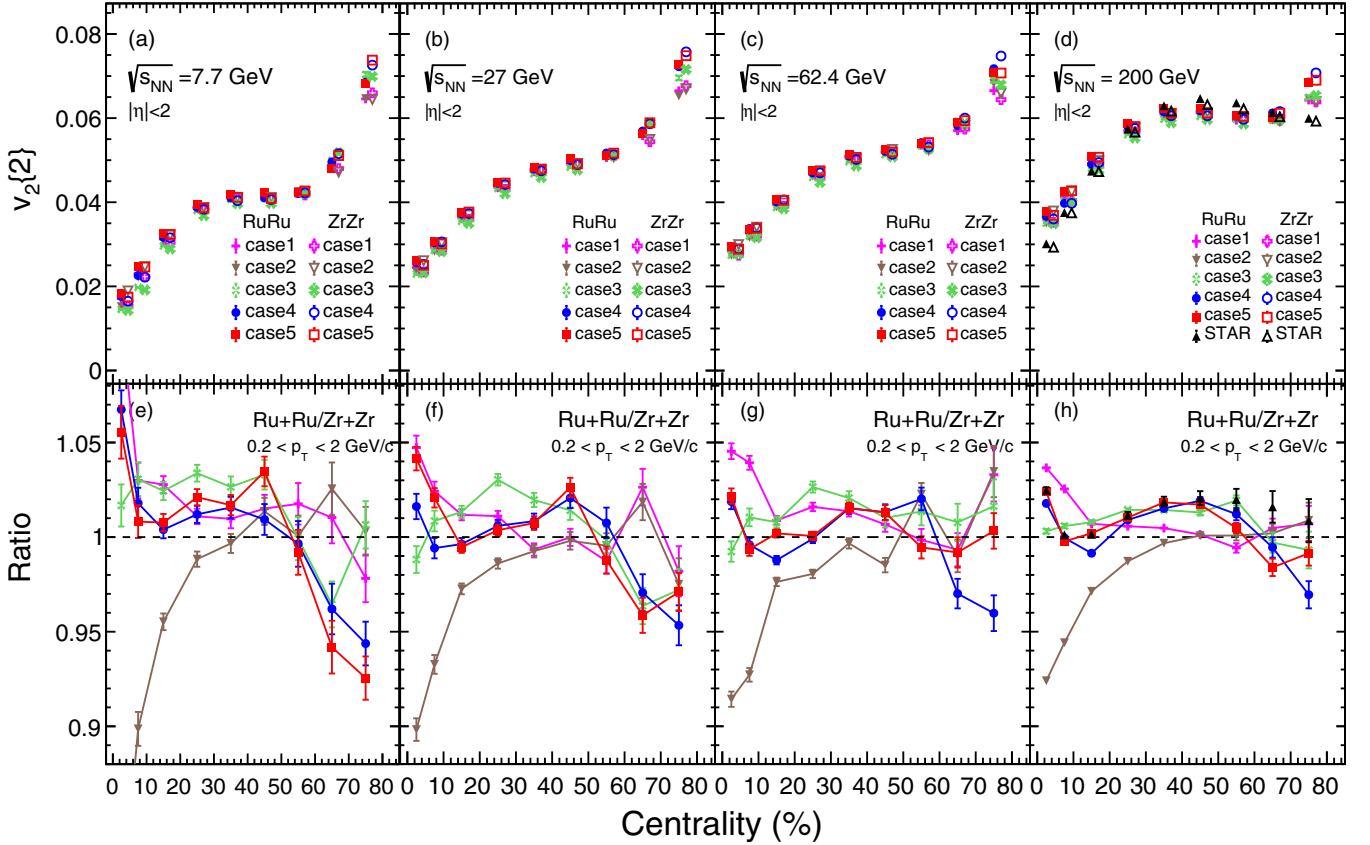


FIG. 3. (Upper panels) Elliptic flow $v_2\{2\}$ measurements for five cases in isobar collisions at $\sqrt{s_{NN}} = 7.7, 27, 62.4$ and 200 GeV as a function of centrality by using two-particle correlations. The solid and open symbols represent measurements for Ru+Ru and Zr+Zr collisions, respectively. The STAR data [4] for isobar collisions at $\sqrt{s_{NN}} = 200$ GeV are also shown for comparison. The data points are shifted along the x axis for clarity. (Lower panels) The ratios of v_2 in Ru+Ru over Zr+Zr collisions. The statistical uncertainties are represented by lines.

in central (less than 20% centrality) isobaric collision systems, which means that the larger quadrupole deformation β_2 of nucleon distribution is, the larger its $v_2\{2\}$ is. Comparing with the STAR experimental results [4], Case 1 is more consistent with the data in the most central collisions, Case 3 is more consistent with them in mid-central collisions, while Case 4 and Case 5, which take account of both the deformation and the neutron skin effect, are almost consistent with the STAR data in all centralities. It can be seen that the influences of the parameter settings are consistent with the conclusion in Ref. [50], and this also prompts the investigation of the beam energy dependence of the effect from the initial geometry properties.

It was also observed that the ratios of $v_2\{2\}$ are enhanced at lower energies in isobar collisions, but the five settings have different performances at different centralities. As shown in Fig. 4(b), in the central collisions (0–5%), the absolute value of $v_2\{2\}$ ratios decreases with energy for Case 1, Case 2, Case 4, and Case 5, meaning that the effect of the β_2 to $v_2\{2\}$ ratio, which mainly dominates in the most-central collisions, is magnified at lower energy. Comparing the ratios of these cases, with a larger absolute value of $\Delta\beta_{2,\text{case2}}$ ($\beta_{2,Ru} - \beta_{2,Zr} = -0.15$), the ratios of Case 2 drop more strongly in the central region than the other cases, which indicates that a larger $\Delta\beta_2$ results in a larger $v_2\{2\}$ ratio in central collisions.

In addition, due to the negative contribution to $v_2\{2\}$ ratio from β_3 in the near-central collisions, although the $\Delta\beta_2$ of Case 4 ($\Delta\beta_{2,\text{case4}} = 0.092$) and Case 5 ($\Delta\beta_{2,\text{case5}} = 0.102$) are larger than that of Case 1 ($\Delta\beta_{2,\text{case1}} = 0.07$), their $v_2\{2\}$ ratio is still smaller than that of Case 1. It also can be seen that the ratio in Case 3, which does not include the deformation description in WS parameters, remains at unity vs energy.

Figure 4(d) shows the ratios of $v_2\{2\}$ with energy in the mid-central collisions (20–50%). It can be seen that the ratio of Case 3 decreases with energy, while the other cases show a nonmonotonic energy dependence of ratios. Since the neutron skin effect (i.e., Δa) is mainly manifested in the mid-central collisions, the behavior of Case 3 in Fig. 4(d) indicates that the influence of the neutron skin effect on the ratio of $v_2\{2\}$ is enhanced at low energy in the mid-central collisions. For Case 4 and Case 5, the ratios of $v_2\{2\}$ show a nonmonotonic energy dependence in this collision energy region because both sets of WS parameters contain not only the neutron skin effect but also octupole deformation β_3 . Since in the near-central collisions β_3 has a negative contribution to $v_{2,Ru}/v_{2,Zr}$ and in the mid-central collisions Δa has a positive contribution, the two factors conspire to produce the nonmonotonic energy dependence of ratios in this centrality region (20–50%). The ratios of $v_2\{2\}$ present a minor difference for Case 1 and Case 2 at different energies in this centrality region, because the

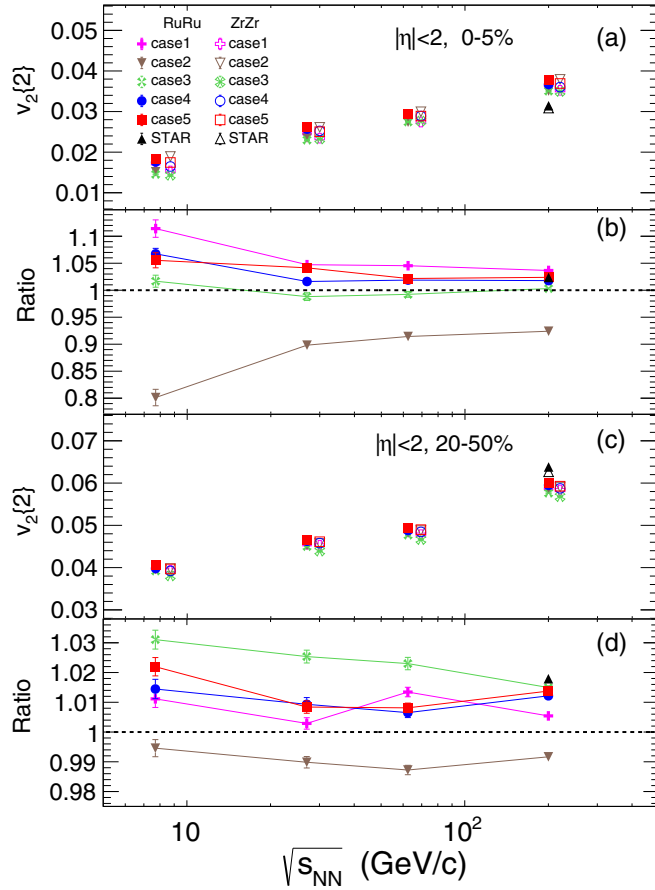


FIG. 4. (a) Elliptic flow $v_2\{2\}$ measurements for five cases in the most central isobar collisions as a function of energy by using two-particle correlations. (b) The ratios of $v_2\{2\}$ in Ru+Ru over Zr+Zr collisions in the most central collisions. (c) Elliptic flow $v_2\{2\}$ measurements for five cases in mid-central isobar collisions as a function of energy by using two-particle correlations. (d) The ratios of $v_2\{2\}$ in Ru+Ru over Zr+Zr collisions in mid-central collisions. For (a) and (b), the STAR data [4] for isobar collisions at $\sqrt{s_{NN}} = 200$ GeV are also shown for comparison. The data points are shifted along the x axis for clarity, and the statistical uncertainties are represented by lines.

quadrupole deformation β_2 has little effect on $v_2\{2\}$ ratios in the mid-central collisions.

The trend of $v_2\{2\}$ ratios at different energies with different centrality reconfirms that the effect of quadrupole deformation β_2 on $v_2\{2\}$ ratios mainly occurs in the most-central collisions, the octupole deformation β_3 dominates in the near-central collisions, and the impact of neutron skin effect on $v_2\{2\}$ ratios mainly happens in the mid-central collisions.

The above results tell us that each nuclear structural factor could result in a larger difference of CME background at low energy. However, due to the negative contribution from β_3 to the $v_{2,Ru}/v_{2,Zr}$ ratio in the near-central collisions, the monotonic energy dependence of the v_2 ratio is weakened at 0–5% and 20–50%. Therefore, we suggest that the energy dependence of the ratio for isobar collisions be studied in extremely ultracentral collisions (0–1%) [51] in the future,

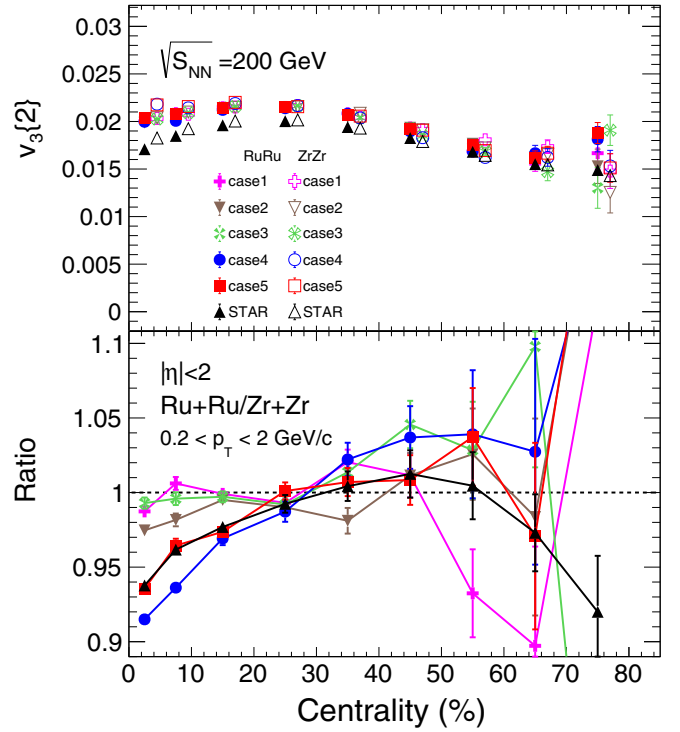


FIG. 5. Upper panels: Triangular flow $v_3\{2\}$ for five cases in isobar collisions at $\sqrt{s_{NN}} = 200$ GeV as a function of centrality by using two-particle correlations. The STAR data [4] for isobar collisions at $\sqrt{s_{NN}} = 200$ GeV are also shown for comparison. The data points are shifted along the x axis for clarity. Lower panels: The ratios of v_3 in Ru+Ru over Zr+Zr collisions. The statistical uncertainties are represented by the bars on dots.

which can avoid the offset of the β_3 to v_2 ratio to obtain a stronger monotonic energy dependence. At the same time, it can solve the problem that the centrality classes of two colliding nuclei are not completely aligned at low energy.

On the other hand, perhaps the lower energy collisions are more suitable for us to study the nuclear structure of $^{96}_{44}\text{Ru}$ and $^{96}_{44}\text{Zr}$ because of stronger signal than at higher energy. In other words, it is worth performing a beam energy scan of isobaric collisions to constrain the nuclear structure parameters or to distinguish the CME background from nuclear structure.

We also investigate the effect of the quadrupole deformation β_2 and octupole deformation β_3 on the triangular flow $v_3\{2\}$ at mid-pseudorapidity ($|\eta| < 2$) as a function of centrality at $\sqrt{s_{NN}} = 200$ GeV, as shown in Fig. 5. From the upper panels of Fig. 5, it is seen that the calculated $v_3\{2\}$ are close to the STAR data [4] for five settings, and the lower panels of Fig. 5 showing the results of Case 4 and Case 5, which include the octupole deformation β_3 , are most similar to STAR data in central collisions. The above results are consistent with the conclusion in Ref. [29] that β_2 has an effect on v_2 but does not on v_3 , and β_3 has a significant effect on $v_3\{2\}$ in central collisions. On the other hand, there exists a similar effect of the chain or triangle structure for an α -clustering nucleus like ^{12}C on v_2 and v_3 , which was observed in our previous work [52]; i.e., the chain structure

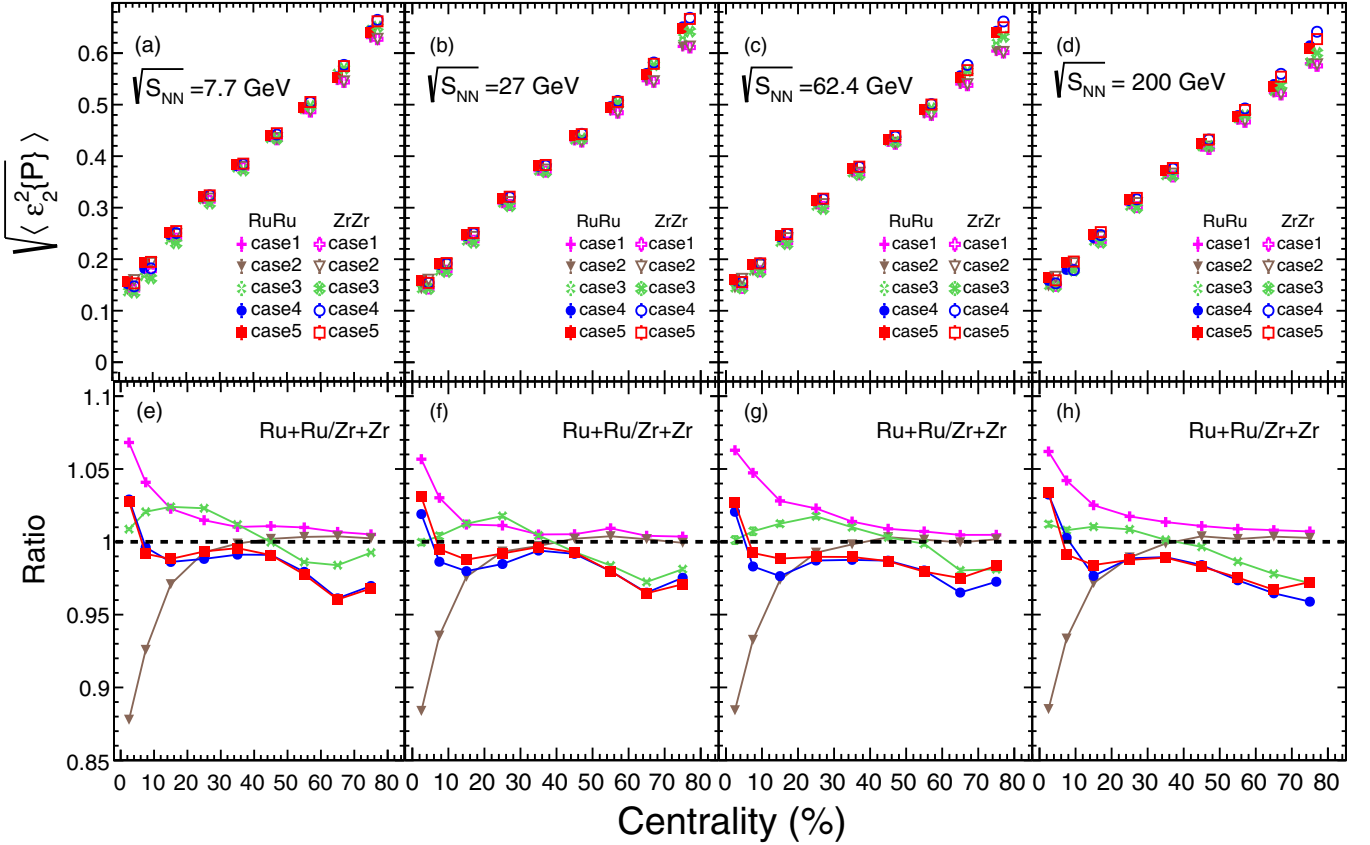


FIG. 6. Upper panels: Eccentricity ε_2 for three cases in isobar collisions at $\sqrt{s_{NN}} = 7.7, 27, 62.4,$ and 200 GeV as a function of centrality. The solid and open symbols represent measurements for Ru+Ru and Zr+Zr collisions, respectively. The data points are shifted along the x axis for clarity. Lower panels: The ratios of ε_2 in Ru+Ru over Zr+Zr collisions. The statistical uncertainties are represented by bars on dots.

has an effect on v_2 but does not on v_3 , but triangle structure has a significant effect on v_3 . Actually, both phenomena induced by the above deformations and clustering structures are essentially related to the transformation from initial-state geometric structure and fluctuation [53] to final-state momentum space.

C. The initial geometry

Next, we want to find whether the differences in final state measurements due to the effects of nuclear structure are already implicit in the early stages after isobar collisions. The initial geometry of a nucleus-nucleus collision can be characterized by eccentricity, which represents the initial geometric anisotropy of the collision zone in the transverse plane (perpendicular to the beam direction). The definition of eccentricity for n th harmonics in the coordinate space of the initial partons [54] for a single collision event is given in the following form [55,56]:

$$\varepsilon_n\{P\} = \frac{\sqrt{\langle r^n \cos(n\varphi) \rangle^2 + \langle r^n \sin(n\varphi) \rangle^2}}{\langle r^n \rangle}, \quad (3)$$

where r and φ are the position and azimuthal angle of each initial parton in the transverse plane. In practice, the event averaged eccentricity coefficients $\langle \varepsilon_n\{P\} \rangle$ are used to

characterize the initial geometry asymmetry, and we mainly focus on the ε_2 in this study.

The upper panels of Fig. 6 show the $\sqrt{\langle \varepsilon_2^2 \rangle}$ for five cases in isobar collisions at $\sqrt{s_{NN}} = 7.7, 27, 62.4,$ and 200 GeV as a function of centrality, and the $\sqrt{\langle \varepsilon_2^2 \rangle}$ for five settings are close to each other at different centralities. The lower panels of Fig. 6 present the $\sqrt{\langle \varepsilon_2^2 \rangle}$ ratios between Ru+Ru and Zr+Zr collisions. As expected, the shape of $\sqrt{\langle \varepsilon_2^2 \rangle}$ ratios is similar to the above presented flow ratios for the five settings at different centralities; i.e., the effect of deformation on eccentricity mainly occurs in the central collisions, while the effect of neutron skin on eccentricity mainly dominates in mid-central collisions. This illustrates that part of the contribution to the difference on CME backgrounds in Ru+Ru and Zr+Zr collisions originates from the effect of nuclear structure on the initial geometry after collisions.

In addition, we can see that the shape of the $\sqrt{\langle \varepsilon_2^2 \rangle}$ ratio have no significant changes at different energy as shown in Fig. 7 for the centrality ranges of 0–5% and 20–50% with five settings of nuclear structure parameters. The energy independence of $\sqrt{\langle \varepsilon_2^2 \rangle}$ ratios is opposite to the previous situation of v_2 ratios, suggesting that it is energy dependent for the

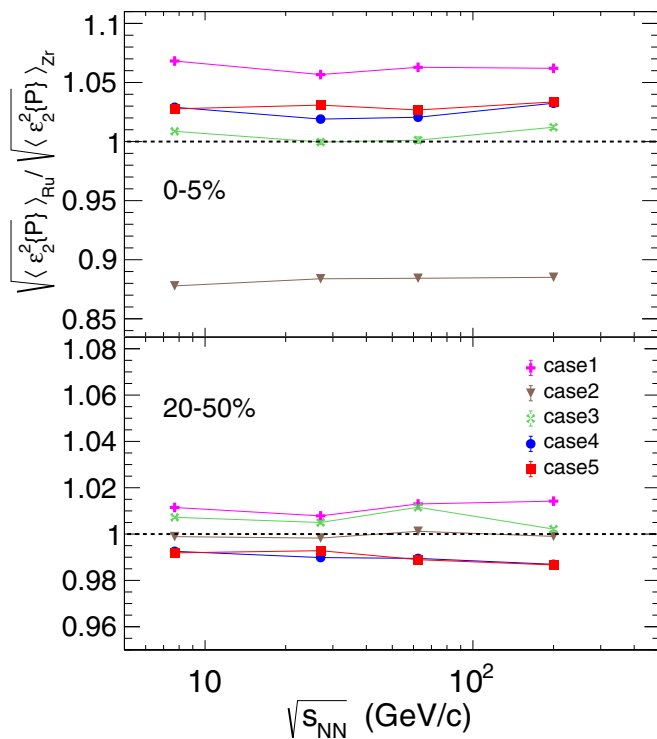


FIG. 7. Upper panels: The ratios of $\sqrt{\langle \varepsilon_2^2 \rangle}$ in Ru+Ru over Zr+Zr collisions in the most central collisions. Lower panels: The ratios of $\sqrt{\langle \varepsilon_2^2 \rangle}$ in Ru+Ru over Zr+Zr collisions in mid-central collisions. The statistical uncertainties are represented by bars on dots.

transition efficiency from initial geometry asymmetry to final momentum space. And the energy dependence of the v_2 ratios via a transport model, such as AMPT, indicates the hydrodynamical-like evolution mechanism in the collisions [57–59].

IV. CONCLUSION AND OUTLOOK

The recent STAR measurement of the final state observables confirmed the differences in nuclear structure between Ru and Zr systems. By comparing the simulation results in Ru+Ru and Zr+Zr collisions from the AMPT model with the STAR data, we found that these differences can be explained by different quadrupole deformation β_2 , octupole deformation β_3 , as well as the neutron skin. These results are consistent with previous studies [26,29,30,50,51,60]. Our results

reconfirm the centrality dependence of the difference in final state observables between Ru+Ru and Zr+Zr collisions on nuclear structure [50]; i.e., the positive contribution to $v_{2,Ru}/v_{2,Zr}$ of the quadrupole deformation β_2 and the neutron skin effect occurs in the most-central collisions and the mid-central collisions, respectively, and the negative contribution to $v_{2,Ru}/v_{2,Zr}$ of octupole deformation β_3 happens in the near-central collisions. This conclusion was supported more strongly by subsequent investigation of the energy dependence of v_2 ratios in Ru+Ru/Zr+Zr in the central collisions and the mid-central collisions, respectively, which showed that each nuclear structure factor magnifies the difference of v_2 at lower energy in the collision region where it dominates. The results of the energy dependence of v_2 ratios also indicate that larger CME backgrounds can be generated in lower energy from Ru+Ru and Zr+Zr collisions.

The study of eccentricity ratios of two systems tells us that part of the CME background difference originates from the difference of initial geometry in Ru+Ru and Zr+Zr collisions. The fact that eccentricity ratios are independent of energy shows that the energy dependence of the difference in v_2 ratio is also influenced by the dynamical evolution of the collision zone.

If background differences due to the different nuclear structures can be more accurately predicted, we might be able to isolate them and get a clean signal of the CME effect. Fortunately, a more precise deformation description has been tested in some work and seems successful in describing new data of RHIC and LHC experiments [29,61–63]. Our analysis also shows that the background difference caused by each nuclear structural factor in isobar collisions can be magnified at lower energy. As Ref. [29] pointed out, isobar collisions can be used as a precision tool to measure the shape of nuclei, and this may be easier to do at lower energy.

ACKNOWLEDGMENTS

This work was supported in part by the National Natural Science Foundation of China under Contracts No. 11875066, No. 11890710, No. 11890714, No. 12061141008, No. 11925502, No. 11975078, and 12147101, National Key R&D Program of China under Grants No. 2018YFE0104600 and No. 2016YFE0100900, the Strategic Priority Research Program of CAS under Grant No. XDB34000000, and the Guangdong Major Project of Basic and Applied Basic Research No. 2020B0301030008.

[1] D. Kharzeev, R. D. Pisarski, and M. H. G. Tytgat, *Phys. Rev. Lett.* **81**, 512 (1998).
 [2] D. Kharzeev and R. D. Pisarski, *Phys. Rev. D* **61**, 111901(R) (2000).
 [3] P. Morley and I. Schmidt, *Z. Phys. C: Part. Fields* **26**, 627 (1985).
 [4] M. S. Abdallah *et al.* (STAR Collaboration), *Phys. Rev. C* **105**, 014901 (2022).
 [5] V. Skokov, A. Y. Illarionov, and V. Toneev, *Int. J. Mod. Phys. A* **24**, 5925 (2009).

[6] Y. Sun, Y. Wang, Q. Li, and F. Wang, *Phys. Rev. C* **99**, 064607 (2019).
 [7] K. Fukushima, D. E. Kharzeev, and H. J. Warringa, *Phys. Rev. D* **78**, 074033 (2008).
 [8] D. E. Kharzeev, L. D. McLerran, and H. J. Warringa, *Nucl. Phys. A* **803**, 227 (2008).
 [9] D. Kharzeev, *Phys. Lett. B* **633**, 260 (2006).
 [10] Y. C. Liu and X. G. Huang, *Nucl. Sci. Tech.* **31**, 56 (2020).
 [11] J.-H. Gao, G.-L. Ma, S. Pu, and Q. Wang, *Nucl. Sci. Tech.* **31**, 90 (2020).

- [12] D. E. Kharzeev and J. Liao, *Nat. Rev. Phys.* **3**, 55 (2021).
- [13] D. E. Kharzeev, J. F. Liao, S. A. Voloshin, and G. Wang, *Prog. Part. Nucl. Phys.* **88**, 1 (2016).
- [14] R.-H. Fang, R.-D. Dong, D.-F. Hou, and B.-D. Sun, *Chin. Phys. Lett.* **38**, 091201 (2021).
- [15] L.-L. Gao and X.-G. Huang, *Chin. Phys. Lett.* **39**, 021101 (2022).
- [16] F.-Q. Wang and J. Zhao, *Nucl. Sci. Tech.* **29**, 179 (2018).
- [17] H.-H. Peng, J.-J. Zhang, X.-L. Sheng, and Q. Wang, *Chin. Phys. Lett.* **38**, 116701 (2021).
- [18] W. Li and G. Wang, *Annu. Rev. Nucl. Part. Sci.* **70**, 293 (2020).
- [19] J. Zhao and F. Q. Wang, *Prog. Part. Nucl. Phys.* **107**, 200 (2019).
- [20] X.-L. Ren, C.-X. Wang, K.-W. Li, L.-S. Geng, and J. Meng, *Chin. Phys. Lett.* **38**, 062101 (2021).
- [21] J.-N. Rong, L. Chen, and K. Chang, *Chin. Phys. Lett.* **38**, 084501 (2021).
- [22] S. A. Voloshin, *Phys. Rev. C* **70**, 057901 (2004).
- [23] A. Bzdak, V. Koch, and J. Liao, *Phys. Rev. C* **83**, 014905 (2011).
- [24] J. Liao, V. Koch, and A. Bzdak, *Phys. Rev. C* **82**, 054902 (2010).
- [25] F. Wang, *Phys. Rev. C* **81**, 064902 (2010).
- [26] W.-T. Deng, X.-G. Huang, G.-L. Ma, and G. Wang, *Phys. Rev. C* **94**, 041901(R) (2016).
- [27] P. Tribedy (STAR Collaboration), *J. Phys.: Conf. Ser.* **1602**, 012002 (2020).
- [28] J. Adam, L. Adamczyk, J. R. Adams *et al.*, *Nucl. Sci. Tech.* **32**, 48 (2021).
- [29] C. Zhang and J. Jia, *Phys. Rev. Lett.* **128**, 022301 (2022).
- [30] H.-J. Xu, X. Wang, H. Li, J. Zhao, Z.-W. Lin, C. Shen, and F. Wang, *Phys. Rev. Lett.* **121**, 022301 (2018).
- [31] Z.-W. Lin, C. M. Ko, B.-A. Li, B. Zhang, and S. Pal, *Phys. Rev. C* **72**, 064901 (2005).
- [32] Z.-W. Lin and L. Zheng, *Nucl. Sci. Tech.* **32**, 113 (2021).
- [33] A. Adare *et al.* (PHENIX Collaboration), *Phys. Rev. C* **94**, 054910 (2016).
- [34] G.-L. Ma and A. Bzdak, *Phys. Lett. B* **739**, 209 (2014).
- [35] A. Bzdak and G.-L. Ma, *Phys. Rev. Lett.* **113**, 252301 (2014).
- [36] M.-W. Nie, P. Huo, J. Jia, and G.-L. Ma, *Phys. Rev. C* **98**, 034903 (2018).
- [37] H. Wang and J. H. Chen, *Nucl. Sci. Tech.* **32**, 2 (2021).
- [38] X.-N. Wang and M. Gyulassy, *Phys. Rev. D* **44**, 3501 (1991).
- [39] M. Gyulassy and X.-N. Wang, *Comput. Phys. Commun.* **83**, 307 (1994).
- [40] B. Zhang, *Comput. Phys. Commun.* **109**, 193 (1998).
- [41] B.-A. Li and C. M. Ko, *Phys. Rev. C* **52**, 2037 (1995).
- [42] G. Giacalone, J. Jia, and C. Zhang, *Phys. Rev. Lett.* **127**, 242301 (2021).
- [43] Q. Y. Shou, Y. G. Ma, P. Sorensen, A. H. Tang, F. Videbak, and H. Wang, *Phys. Lett. B* **749**, 215 (2015).
- [44] H. Li, H.-J. Xu, J. Zhao, Z.-W. Lin, H. Zhang, X. Wang, C. Shen, and F. Wang, *Phys. Rev. C* **98**, 054907 (2018).
- [45] J. Hammelmann, A. Soto-Ontoso, M. Alvioli, H. Elfner, and M. Strikman, *Phys. Rev. C* **101**, 061901(R) (2020).
- [46] S. Raman, C. W. Nestor, and P. Tikkannen, *At. Data Nucl. Data Tables* **78**, 1 (2001).
- [47] B. Pritychenko, M. Birch, B. Singh, and M. Horoi, *At. Data Nucl. Data Tables* **107**, 1 (2016).
- [48] P. Moller, J. Nix, W. Myers, and W. Swiatecki, *At. Data Nucl. Data Tables* **59**, 185 (1995).
- [49] H.-J. Xu, H. Li, X. Wang, C. Shen, and F. Wang, *Phys. Lett. B* **819**, 136453 (2021).
- [50] J. Jia and C.-J. Zhang, [arXiv:2111.15559](https://arxiv.org/abs/2111.15559).
- [51] G. Nijs and W. van der Schee, [arXiv:2112.13771](https://arxiv.org/abs/2112.13771).
- [52] S. Zhang, Y. G. Ma, J. H. Chen, W. B. He, and C. Zhong, *Phys. Rev. C* **95**, 064904 (2017).
- [53] L. Ma, Y. G. Ma, and S. Zhang, *Phys. Rev. C* **102**, 014910 (2020).
- [54] S. Zhang, Y. G. Ma, J. H. Chen, W. B. He, and C. Zhong, *Eur. Phys. J. A* **54**, 161 (2018).
- [55] B. Alver, B. B. Back, M. D. Baker, M. Ballintijn, D. S. Barton, R. R. Betts, R. Bindel, W. Busza, V. Chetluru, E. Garcia, T. Gburek, J. Hamblen, U. Heinz, D. J. Hofman, R. S. Hollis, A. Iordanova, W. Li, C. Loizides, S. Manly, A. C. Mignerey, R. Nouicer, A. Olszewski *et al.*, *Phys. Rev. C* **77**, 014906 (2008).
- [56] J. Adams *et al.*, *Phys. Rev. C* **72**, 014904 (2005).
- [57] H. Song and U. Heinz, *Phys. Lett. B* **658**, 279 (2008).
- [58] T. A. Trainor, *Mod. Phys. Lett. A* **23**, 569 (2008).
- [59] C. Shen and L. Yan, *Nucl. Sci. Tech.* **31**, 122 (2020).
- [60] G. Giacalone, J. Jia, and V. Somà, *Phys. Rev. C* **104**, L041903 (2021).
- [61] J. Jia, *Phys. Rev. C* **105**, 014905 (2022).
- [62] B. Bally, M. Bender, G. Giacalone, and V. Soma, *Phys. Rev. Lett.* **128**, 082301 (2022).
- [63] G. Giacalone, B. Schenke, and C. Shen, *Phys. Rev. Lett.* **128**, 042301 (2022).